coatings

MDPI

Article

Effect of Energy Density on the Microstructure and Wear Resistance of Nickel-Based WC Coatings by Laser Cladding of Preset Zr702 Alloy Plates

Guangsheng Zhang [1,2,3], Aixin Feng [1,2,3,*], Pu Zhao [1], Xiaoming Pan [1] and Huibin Feng [4]

[1] College of Mechanical and Electrical Engineering, Wenzhou University, Wenzhou 325035, China; 20461439004@stu.wzu.edu.cn (G.Z.)
[2] Rui'an Graduate College, Wenzhou University, Wenzhou 325206, China
[3] Zhejiang Provincial Key Laboratory of Laser Processing Robots, Machinery Industry Key Laboratory of Laser Processing and Testing, Wenzhou 325035, China
[4] Zhejiang Linuo Fluid Control Technology Co., Ltd., Wenzhou 325200, China
* Correspondence: aixfeng@wzu.edu.cn; Tel.: +86-0577-8659-6099

Abstract: This study aimed to evaluate the microstructure and wear resistance of laser cladding coatings with different energy densities in the case of a preset 0.5 mm thick Zr702 alloy plate to determine the specific present form of Zr elements and the optimal laser energy density. Thereby, microscopic characterization and performance tests were carried out by the microhardness tester, X-ray diffraction analysis (XRD), scanning electron microscopy (SEM), and tribometer. The results showed that, at different energy densities, the Zr elements in the coating were mainly in the form of ZrC and (Zr,W)C, which are hard particles with high wear resistance, and diffusely distributed in the coating to have second-phase-strengthening effects. Moreover, when the energy density was 28.3 J/mm^2, the coating was well fused and had the highest microhardness of 936.4 $HV_{0.2}$. The wear rate of the coating was the lowest at 90.8 μm^3/(m·N). The wear was characterized by hard particle spalling and abrasive wear.

Keywords: laser cladding; energy density; Zr702 alloy; (Zr,W)C; wear resistance; microstructure

Citation: Zhang, G.; Feng, A.; Zhao, P.; Pan, X.; Feng, H. Effect of Energy Density on the Microstructure and Wear Resistance of Nickel-Based WC Coatings by Laser Cladding of Preset Zr702 Alloy Plates. *Coatings* **2023**, *13*, 826. https://doi.org/10.3390/coatings13050826

Academic Editor: Alina Vladescu

Received: 13 March 2023
Revised: 17 April 2023
Accepted: 19 April 2023
Published: 25 April 2023

1. Introduction

Solar energy has the advantages of being environmentally friendly, sustainable, and green [1] and is one of the important development directions for building a world of clean energy. Silicon-based solar batteries occupy more than 90% of the market share in the solar batteries field due to their excellent stability [2]. Polysilicon is the most-common raw material for the production of silicon-based solar batteries. However, the sealing surfaces of control valves used in the polysilicon preparation process are susceptible to failure because of wear under the harsh conditions of ultra-hard silicon powder particles (Mohs hardness of 7.5), resulting in long downtimes of the polysilicon production line for maintenance, which greatly increases the costs of production and time. Therefore, the development of ultra-high wear-resistant coatings for control valve sealing surfaces in the field of polysilicon preparation has become a key problem to be solved.

Strengthening treatment on traditional control valve sealing surfaces mainly uses arc welding, plasma arc welding, and other overlay welding technology. However, it has the disadvantageous problems of cracking, an uneven hardness distribution, and coarse crystals. As a laser cladding technology based on overlay welding technology, it has received extensive attention and research from experts and scholars at home and abroad because of its dense microstructure [3], fine grain size [4], and good mechanical properties [5]. From the perspective of the addition and in situ generation of hard phases, a large number of scholars have carried out research on reinforcing phases such as WC, SiC,

NbC, Al_2O_3, and BN [6–10]. However, it is worth noting that compounds of Zr such as ZrB_2 (microhardness of 22 GPa), ZrN (19.6 GPa), ZrC (29.2 GPa), and ZrO_2 (12 GPa) have excellent mechanical properties with high hardness. Yang, C. and X. Li [11,12] investigated the effect of different ZrN additions on the microstructure and properties of TC11 titanium alloy by laser cladding, and the results showed that the addition of ZrN can greatly improve the wear resistance of the coating. Y.-W. Yong [13] showed that a nickel-based alloy coating with ZrO_2 + C was melted on AISI 1045, and the results showed that fine ZrC particles were generated in situ in the coating and the wear resistance was 2.7 times that of Ni25. Guo, J. [14] showed that a 35 wt.% ZrB_2 + Ni60A coating was produced on pure titanium substrates, and he found that the coating had higher hardness than conventional NiCrBSi composite coatings. The addition of ZrB_2 effectively reduced the adhesive wear of the NiCrBSi coatings. Liu Kun [15] prepared NiCrBSi coating on a Zr702 substrate, and the results showed that the coating microstructure consisted of NiZr solid solution and bulk reinforcement including $NiZr_2$, $Zr_5(SixNi_{1-x})_4$, and ZrB_2. The average microhardness reached 1200–1300 $HV_{0.2}$, nearly seven times that of the Zr702, overturning the usual thinking that lower dilution is better in laser cladding.

Currently, no studies have been found to improve the properties with Zr702 in nickel-based coatings. Therefore, this paper creatively adopted a preset Zr702 alloy plate to investigate the effect of different energy densities on the microstructure and wear resistance of the laser cladding of Ni60A + 20 wt.% WC composite coatings, providing a reference for the research and application in the field of laser cladding of preset high-performance alloy plates. Figure 1 shows the schematic diagram and the expected Microstructure of the laser melting of the preset Zr702 plates.

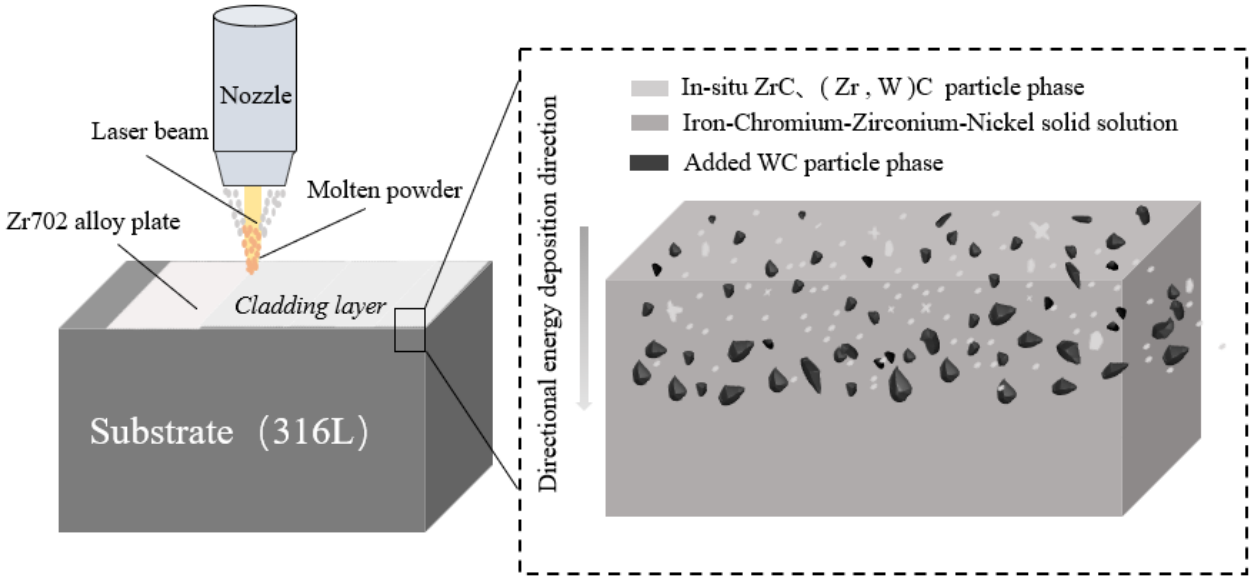

Figure 1. Schematic diagram and expected microstructure for laser cladding of preset Zr702 alloy plates.

2. Materials and Methods

The bond phase powder used in this experiment is the 45–106 μm Ni60A alloy powder(Xindian Materials Co., Ltd., Shanghai, China). The hard phase is the 150–325 mesh powders of WC (Nangong Xindun Alloy Welding Material Spraying Co., Ltd., Xingtai, China). Zr702 (Shanxi TOP Metal Co., Ltd., Shanxi, China) is a 0.5 mm-thick zirconium hafnium alloy plate with dimensions of 90 mm × 60 mm. 316 L was selected as the substrate with dimensions of 90 mm × 60 mm × 9 mm. After presetting the Zr702 alloy, the coating was prepared by Model RFL-C4000 fiber-coupled semiconductor laser cladding equipment with a powder mixture of Ni60A + 20 wt.% WC under an argon gas-protected environment. The laser specifications are as follows: a wavelength of about 1064 nm and a

peak power of 4000 W. The friction wear test of the coating was performed by a tribometer (UMT-5, Bruker, Billerica, MA, USA) with a wear time of 30 min under the parameters of a normal load of 15 N at room temperature, a reciprocating stroke of 2 mm, a frequency of 5 Hz, and a Si_3N_4 friction pair of 4 mm in diameter. After taking the 3D morphology of wear surface of the coating with the PCB 3D optical profiler, the wear loss volume was calculated by the Vision software. The specific composition of the experimental material is shown in Table 1. The microhardness from the top of the cladding layer to the substrate was measured by a microhardness tester (MVA-402TS), and the load and duration used for each hardness measurement were 200 g and 20 s, respectively. Microhardness experiments were performed three times. XRD (FRINGE EV, LANScientific, Suzhou, China) and SEM (Nova 200 Nano SEM, FEI, Hillsboro, United States) with energy dispersive spectrometry (EDS, FEI, Hillsboro, OR, USA) were used to characterize the microstructure. The laser parameters of the cladding coating were designed as shown in Table 2.

Table 1. Elemental composition (wt.%) of Ni60A and Zr702.

Element	Zr + Hf	Hf	Si	Cr	Fe	Ni	C	B	N	H	O
Zr702 alloy plates	≥99.2	≤4.5			0.2		0.05		0.025	0.005	0.16
Ni60A power			4.3	13.7	4.43	Bal.	0.6	3.18			

Table 2. Experimental laser parameters design for composite coatings.

Sample	Off-Focus Volume (mm)	Laser Power (W)	Scanning Speed (mm/s)	Feed Rate (r/min)	Beam Diameter (mm)	Energy Density (J/mm^2)
S1	2.5	800	6	16	3	22.6
S2	2.5	1000	6	16	3	28.3
S3	2.5	1300	6	16	3	36.8
S4	2.5	1500	6	16	3	42.5

3. Results and Discussion

3.1. Section Morphology and Microhardness

Scholars have opined that a large dilution of the coating will weaken the mechanical properties [16], generally not exceeding 20%. However, for this experiment, the dilution rate had to be increased to melt through the Zr702 alloy plate and melt a small portion of the 316 L substrate to achieve good metallurgical bonding of the dissimilar metals under the condition of preset 0.5 mm-thick Zr702 alloy plates. As can be seen from Figure 2, there was no obvious cracking in the overall cladding section and only a few pores. When the laser energy density was 22.6 J/mm^2, the S1 coating just melted through the Zr702 alloy plate and melted the 316 L substrate with less dilution into the melt pool. In Figure 2c, the article defines the melt height of the cladding layer as L_1 and the melt depth as L_2. The melt height and width were measured by the LEXT software (OLS4100 3.1.7) attached to the confocal microscope, and the dilution rates of the coatings in Figure 2a–d were 33.4%, 38.6%, 43.9%, and 48.8% respectively. The dilution rate increases linearly with increasing laser energy density.

Figure 3 presents microhardness diagrams of the top of the laser cladding coating of preset Zr702 to the 316 L substrate at different laser energy densities. The average microhardness value of the S1 to S4 coatings are 885.8 $HV_{0.2}$, 936.4 $HV_{0.2}$, 778.9 $HV_{0.2}$, and 736.2 $HV_{0.2}$, respectively. With increasing energy density, the microhardness showed a trend of increasing and then decreasing, which is consistent with the hardness trend in literature studies [17]. When the energy density was 22.6 J/mm^2, the S1 coating was not sufficiently melted and recrystallized with less eutectic phase precipitation and a more γ-(Fe,Ni) solid solution. The insufficiently melted particles slowed down the Marangoni convection inside the melt pool; dislocations at the grain boundaries were hindered and stresses were more concentrated, resulting in poor coating quality and a lower hardness of the S1

coating. When the energy density was 28.3 J/mm^2, the S2 coating microhardness reached a maximum value of 936.4 $HV_{0.2}$. With the increasing energy density, the microhardness of the S3 and S4 coatings gradually decreased, which was mainly attributed to the following two factors. On the one hand, the increase in energy density inevitably led to the dilution of 316 L base material elements into the coating, which weakened the mechanical properties of the coating [18]. On the other hand, due to the increasing energy input, the grain size was coarse, and the hardness decreased according to the Hall–Petch equation [19].

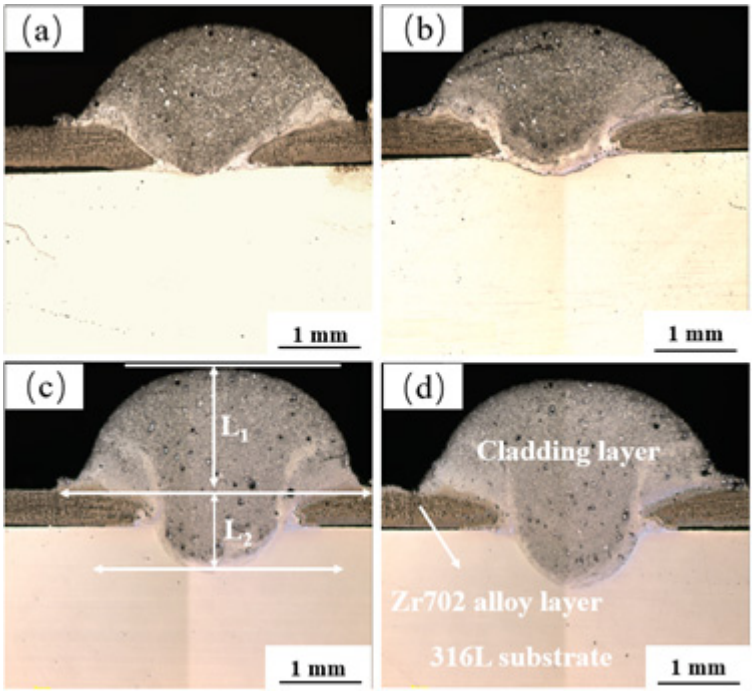

Figure 2. Single-pass cross-sectional morphology of the cladding layer at different energy densities: (**a**) S1; (**b**) S2; (**c**) S3; (**d**) S4.

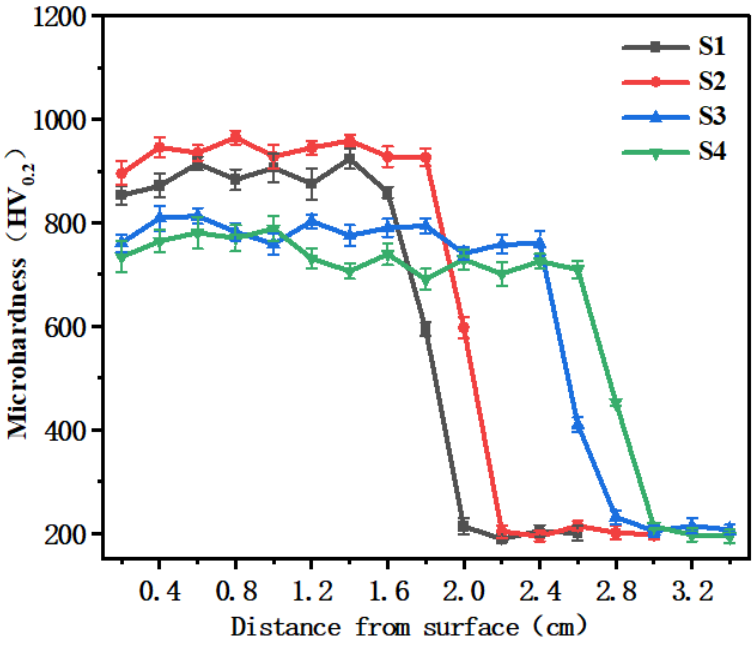

Figure 3. Microhardness diagram of preset Zr702 alloy coating at different energy densities.

3.2. Microstructure Analysis

3.2.1. Composition of the Material Phase

To reveal the composition of the coating phase, the XRD diffraction analysis was carried out. By comparing the PDF standard cards, the physical phases are shown in Figure 4. Although coatings with different laser energy densities were obtained, the main phases of the individual coatings differed little and were γ-(Fe, Ni), Ni_3Fe, WC, $Cr_{23}C_6$, Fe_3N, (Zr,W)C, $Ni_{10}Zr_7$, ZrC, and $M_{23}C_6$. As typical hard phases, $Cr_{23}C_6$ and ZrC play a precipitation-strengthening role in the coating. At high temperatures, the WC in the coating decomposed to produce free C. As the Zr and Hf elements have similar chemical properties, the free C and the Hf and Zr atoms in the Zr702 alloy were bonded to produce HfC and ZrC at specific temperatures. When the energy density was 28.3 J/mm^2, the new ZrN and ZrO_2 phases in the S2 coating had high hardness and chemical stability, and the coating wear resistance was enhanced to a certain extent. Unlike the literature [20], due to the low introduction of Zr, there were no multiple intermetallic compounds of NiZr, Ni_2Zr, and $Ni_{10}Zr_7$ as mentioned in the literature, and only $Ni_{10}Zr_7$ was detected by XRD in this experimental coating. The average grain sizes calculated from S1 to S4 by the Debye–Scherrer formula [21] were 27 nm, 27.9 nm, 29.6 nm, and 31.5 nm, respectively.

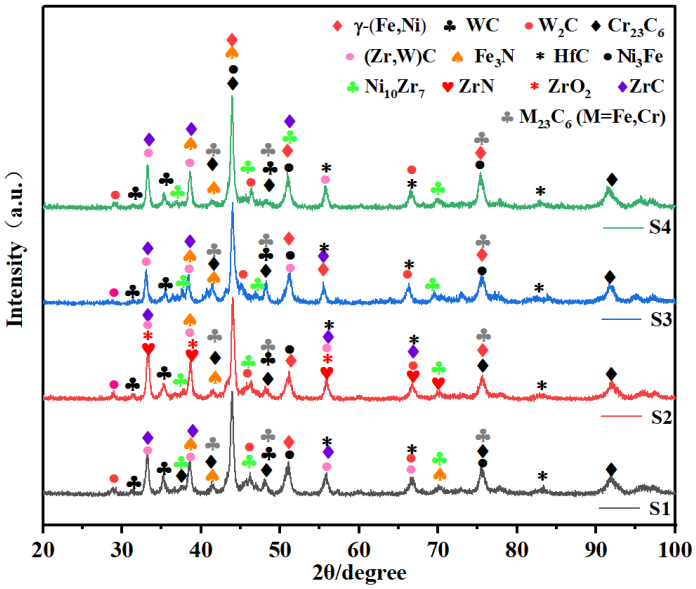

Figure 4. XRD diffraction results of S1 to S4 cladding coatings at different energy densities.

3.2.2. Microstructure and (Zr,W)C Phase Evolution Pattern

In Figure 5, the microstructures of S2 and S4 cladding coatings all contain the γ-(Fe,Ni) solid solution, eutectic organization ($M_{23}C_6$, $Cr_{23}C_6$, $Ni_{10}Zr_7$), incompletely decomposed WC, and diffusely distributed ZrC, (W,Zr)C. Table 3 shows the EDS point scan results of each marker in Figure 5. The flower-like Marker 1 and small particle Marker 2 in Figure 5 contain a large amount of W and Zr elements, and about 2.4 wt.% of the Hf elements were detected for both of them. Based on the facts that the HfC phase was detected in XRD and the literature on the generation of (W,Zr)C at high temperatures [22], Markers 1 and 2 can be further analyzed to determine (W,Zr)C, as well as trace amounts of HfC. As can be seen in Figure 5(a1), Markers 3 and 4 showed serrated and needle-like morphologies. The results of the point scan showed that the content of each element in the two markers was similar, mainly containing W, Cr, and a small amount of C. Therefore, Markers 3 and 4 were judged as the incompletely decomposed WC and the carbide of Cr formed around the WC. Since free C is the first to form a ceramic phase with Zr and Hf, then, the C concentration decreases and inhibits the growth of M_7C_3 [23], while fine $M_{23}C_6$ is formed in the eutectic microstructure. Marker 5 contained 76.88 wt.% of Ni elements and a small amount of

Cr, Zr, and Fe elements, so the analysis determined that it was a γ-(Fe, Ni) solid solution containing Cr and Zr. It is noteworthy that the eutectic microstructure (Marker 6) in the region of Figure 5(a2) contains a fence-like tissue, while it was also found in Figure 5(b2). Compared with Marker 5, Marker 6 showed 3.98 wt% of Zr elements and increased Ni elements, and $Ni_{10}Zr_7$ was detected with XRD, so it was judged as the γ-(Fe, Ni) solid solution and surface precipitation of reticulated $Ni_{10}Zr_7$ intermetallic compound.

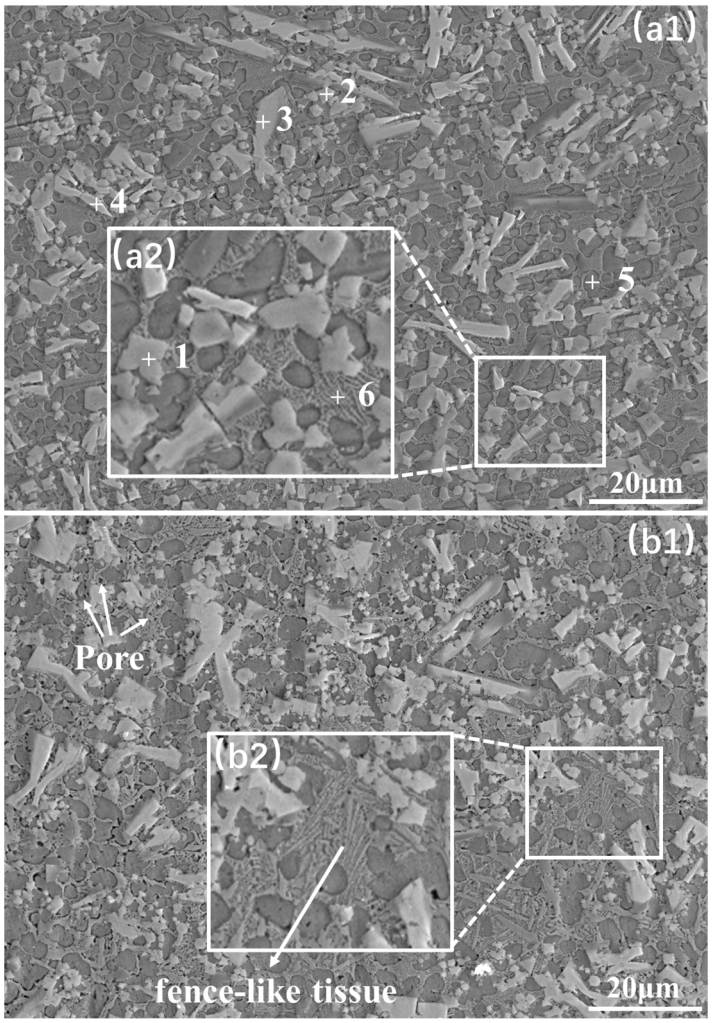

Figure 5. SEM microstructure of the central part of the cladding coating of preset Zr702 alloy at different energy densities: (**a1**,**a2**): S2; (**b1**,**b2**): S4.

Table 3. EDS point scan results at different locations in Figure 5 (wt.%).

Element	1	2	3	4	5	6
C	6.30	5.75	6.61	8.23	0.71	1.07
O	0.52	0.48				
Si					1.13	1.82
Cr	2.25	1.73	18.43	17.80	11.31	3.48
Fe	1.48	1.32	1.61	2.65	7.46	3.07
Ni	17.93	14.45	5.55	7.29	76.88	86.58
Zr	40.82	42.64			0.57	3.98
Hf	2.54	2.40				
W	28.17	31.24	67.8	66.49	1.93	

After presetting a 0.5 mm-thick Zr702 alloy plate, to investigate the distribution of the Zr element in the laser cladding Ni60A-20wt.%WC coating and the chemistry morphology of the Zr element, EDS surface scans were performed on the central microzone of the S2 cladding coating. In Figure 6, it can be seen that the Zr elements are more uniformly distributed, showing irregular shapes such as flowers and squares. Zr (0.167 nm) and W (0.141 nm) have similar atomic radii with a radius difference of only 0.026 nm, implying a certain degree of intercalation. Research work has also reported [24] that the solubility of W in ZrC is approximately 19.5%. Given that the solubility of Zr in WC is almost negligible [25], it can be determined that Markers 2 and 5 in Figure 5(a1) were formed (Zr,W)C around ZrC. The fact that the Zr, W elemental maps did not completely overlap and that ZrC was detected in XRD indicated that ZrC was not completely dissolved to form (Zr,W)C. Therefore, the Zr element ended up in the form of ZrC, (Zr,W)C hard particles as the reinforcing phase of the coating. Since ZrC and (Zr,W)C hard phase particles are highly thermally stable and almost insoluble in the γ-(Fe, Ni) solid solution, most of them were diffusely distributed in the eutectic microstructure between the equiaxed crystals.

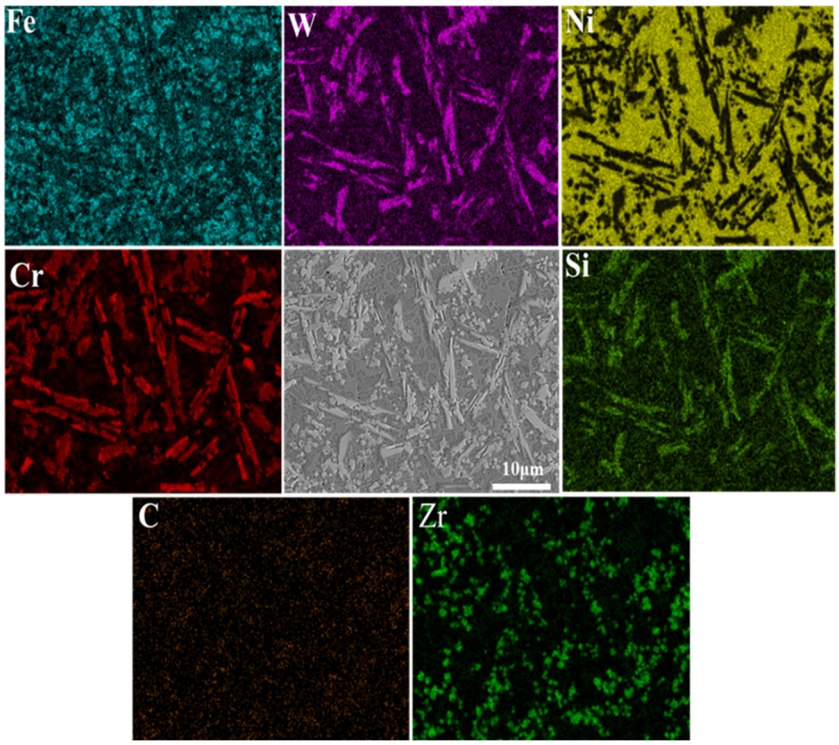

Figure 6. Distribution of elements in the middle area of the S2 cladding coating.

3.3. Wear Properties and Wear Mechanisms

The wear resistance of laser cladding coatings can be evaluated by the coefficient of friction and the wear rate [26]. The distribution of the coefficient of friction with time and the variation of the average coefficient of friction of the laser cladding coating at different energy densities are shown in Figure 7. As can be seen in Figure 7a, the curve is divided into two main stages: the initial ascent stage and the stable stage. The coefficient of friction first underwent a period of oscillatory rise for about 10 min. This was because the surfaces of the coating and the friction pair were not completely smooth, and the tiny convexity on them contacts, resulting in a larger sliding resistance, so the coefficient of friction oscillated up. As the friction proceeded, the surface of the friction pair and the coating was smoother, the wear behavior entered a dynamic and steady stage, and the friction coefficient was more stable.

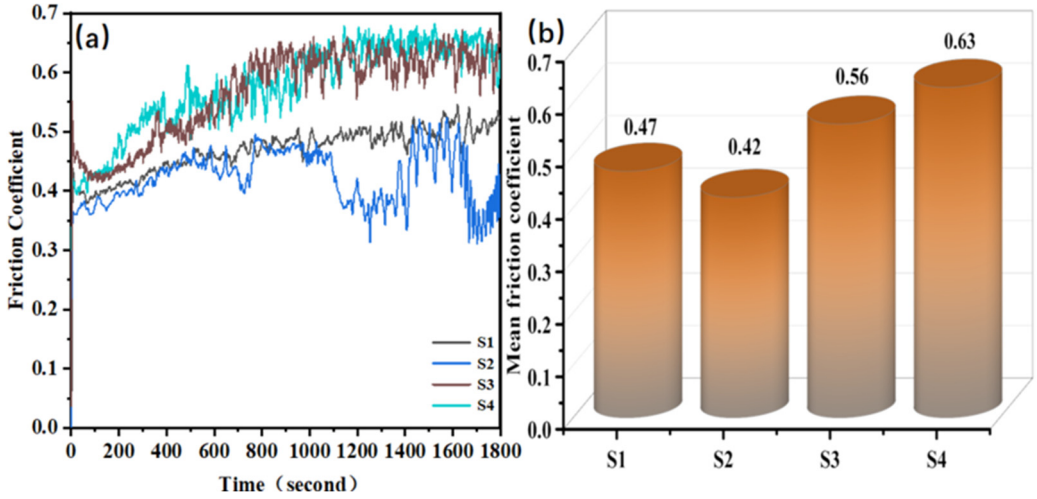

Figure 7. Tribological properties of the S1 to S4 cladding coatings at different energy densities: (**a**) distribution of friction coefficients; (**b**) the average coefficient of friction.

The average coefficients of friction of the coatings S1 to S4 were, respectively, 0.47, 0.42, 0.56, and 0.63, as shown in Figure 7b. The wear rates of the coatings S1 to S4 in Figure 8 were 131.3 $\mu m^3/(m \cdot N)$, 90.8 $\mu m^3/(m \cdot N)$, 145 $\mu m^3/(m \cdot N)$, and 178 $\mu m^3/(m \cdot N)$. Both of them showed a trend of decreasing and then increasing with the increase in the energy density. In Figure 8, it can be seen that the S2 coating had the smallest wear rate of 90.8 $\mu m^3/(m \cdot N)$. It is worth mentioning that the S2 coating appeared to have two suddenly lower coefficients of friction, which was mainly due to the detection of the ZrO_2 phase by XRD and the fact that ZrO_2 is a good self-lubricating ceramic material [27], reducing the coefficient of friction. The wear rate of the S1 and S2 coatings was lower than that of the S3 and S4 coatings. This was mainly because the S1 and S2 coatings contained a higher volume fraction of hard-phase ZrC and HfC particles. When the laser energy density was greater than the critical value of the energy density for melting through Zr702, more 316 L matrix elements diluted into the melt pool, decreasing the mechanical properties of the coating, and there were some ZrC particles in the melt depth part, decreasing the volume fraction of ZrC; therefore, the wear resistance of the S3 and S4 coatings was poorer.

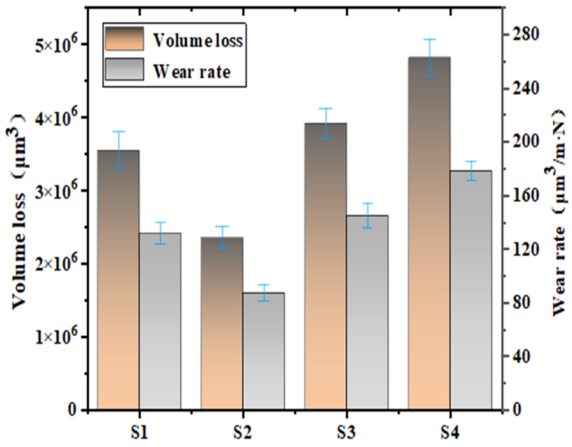

Figure 8. Volume loss and wear rate of the S1 to S4 cladding coatings at different energy densities.

Figure 9(a1,a2) show that the S1 coating surface had large lamellar adhesions and obvious plow grooves. This was because the plow chips of the bonded phase were taken out of the coating under the action of abrasive plowing and crushed by Si_3N_4 against the abrasive part to form the laminate, and the hard particles were shed and acted as abrasive particles, forming "three-body wear" [28]. Figure 9(b1,b2) show that, when the energy

density was 28.3 J/mm^2, the S2 coating had only slight scratches and small hard particle spalling pits. The slight wear behavior above was mainly attributed to the following three aspects: On the one hand, the lattice distortion caused by Zr atoms solidly dissolved in the Ni60A alloy, having solid solution strengthening effects. Therefore, the resistance of the nickel-based solid solution to plastic deformation increased. On the other hand, due to the moderate energy input, the Zr atoms saturated in the γ-(Fe,Ni) solid solution and then segregated at the grain boundaries, forming a large number of Ni-Cr-B-Si eutectics and inhibiting grain growth, having fine crystal strengthening effects; furthermore, a large number of hard phases such as in situ ZrC, (Zr,W)C, and WC particles that are not completely decomposed played an important role in the diffusion-strengthening and second-phase-strengthening effects. From the XRD grain size calculation results, it can be seen that, with the further increase of the energy density, the grain size of the S3 and S4 coatings became larger, decreasing the grain boundary length; the ability to prevent dislocation movement was weakened [29], and the resistance to plastic deformation was reduced. Therefore, as shown in Figure 9(c1,c2,d1,d2), there were obvious plow grooves, spalling pits, and a small number of abrasive chips on the surface of S3. The wear surface morphology of the S4 coating showed wear debris accumulation, mutual parallel abrasion marks, and fatigue cracks formed by the laminae due to cyclic loading, and its wear mechanism was abrasive wear.

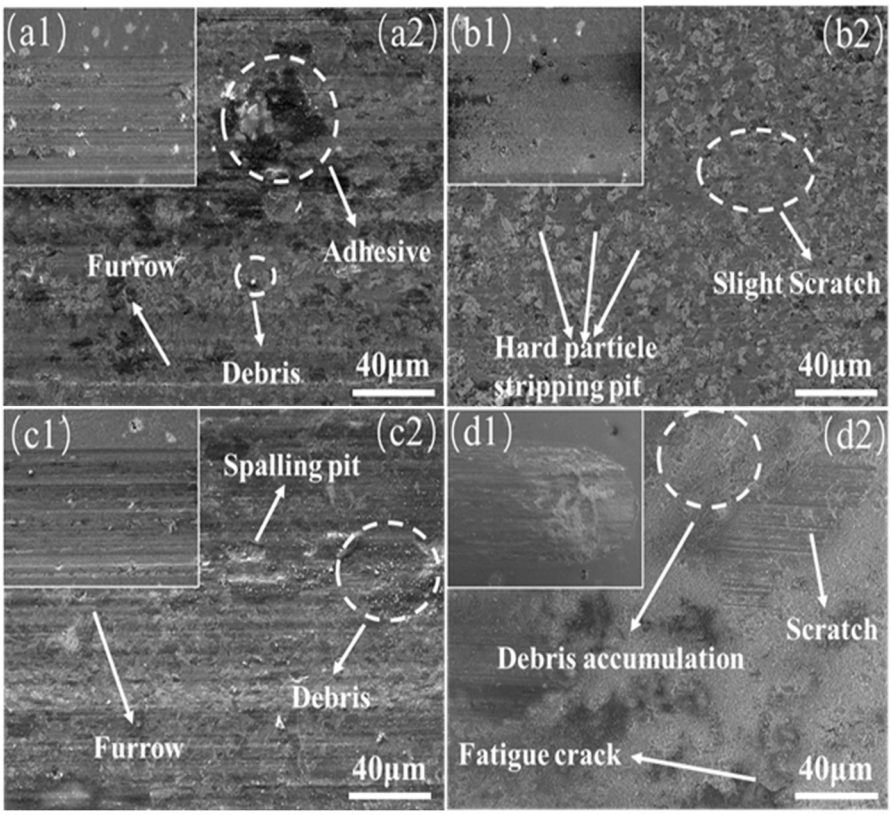

Figure 9. Wear morphology of S1 to S4 cladding coatings at different energy densities: (**a1**,**a2**) S1; (**b1**,**b2**) S2; (**c1**,**c2**) S3; (**d1**,**d2**) S4.

4. Conclusions

In this paper, the effects of different laser energy densities on the microstructure and mechanical properties of Ni60A-20wt.%WC cladding layers were investigated by preplacing a 0.5 mm-thick Zr702 alloy plate on a 316 L substrate, and the main conclusions were as follows:

(1) When the energy density was 28.3 J/mm^2, the coating microhardness was the highest among the specimens of four groups, reaching 936.4 $HV_{0.2}$. With the increase in

energy density, the microhardness of the coating showed a trend of increasing and then decreasing.

(2) After presetting the Zr702 alloy, the coatings with different energy densities were mainly the γ-(Fe,Ni), $M_{23}C_6$, $Cr_{23}C_6$, Ni_3Fe, undecomposed WC, Fe_3N, ZrC, (W,Zr)C, HfC, and $Ni_{10}Zr_7$ phases. The fence-like tissue found in the microstructure was determined to be $Ni_{10}Zr_7$ after EDS point scanning with the XRD results. The Zr element ended up in the form of ZrC, (Zr,W)C hard particles as the reinforcing phase of the coating.

(3) With the increase in the energy density, the wear rate and coefficient of friction showed a trend of decreasing and then increasing. When the energy density was 28.3 J/mm^2, the wear rate of the coating was the lowest at 90.8 μm^3/(m·N). The wear was characterized by hard particle spalling and abrasive wear. The enhancement mechanism was mainly attributed to the low dilution of 316 L into the melt pool, the refinement of the grain, and the formation of a large number of ZrC, (Zr,W)C, which were hard particles with high wear resistance and distributed at the grain boundaries to have second-phase-strengthening effects.

Author Contributions: Conceptualization, G.Z. and P.Z.; methodology, A.F., G.Z. and P.Z.; investigation, A.F. and G.Z.; data curation, X.P. and H.F.; writing—original draft preparation, A.F. and G.Z.; writing—review and editing, A.F., G.Z. and P.Z. All authors have read and agreed to the published version of the manuscript.

Funding: This study was supported by the Natural Science Foundation of Zhejiang Province (LY20E050027), the Major Special Project of Wenzhou Science and Technology Innovation and Tackling Industry (ZG2020029), and the Innovation Fund of Wenzhou University Rui'an Graduate College (YC202212011).

Institutional Review Board Statement: Not applicable.

Informed Consent Statement: Not applicable.

Data Availability Statement: Not applicable.

Conflicts of Interest: The authors declare no conflict of interest. The funders had no role in the design of the study; in the collection, analyses, or interpretation of the data; in the writing of the manuscript; nor in the decision to publish the results.

References

1. Li, P.; Dong, L.; Hu, Z.; Ren, S.; Tan, Y.; Jiang, D.; You, X. Recycling of silicon scraps by electron beam melting coupled with directional solidification and its mechanism of impurity removal. *J. Clean. Prod.* **2022**, *355*, 131716. [CrossRef]
2. Vähänissi, V.; Laine, H.S.; Liu, Z.; Yli-Koski, M.; Haarahiltunen, A.; Savin, H. Full recovery of red zone in p-type high-performance multicrystalline silicon. *Sol. Energy Mater. Sol. Cells* **2017**, *173*, 120–127. [CrossRef]
3. Li, Q.; Li, Y.; Bai, Q.; Chen, C.; Zhao, C.; Liu, Y. Effect of power spinning combined with heat treatment on the organization and wear resistance of high-speed laser cladding coatings. *Mater. Lett.* **2023**, *333*, 133594. [CrossRef]
4. Lian, G.; Liu, Z.; Zhang, Y.; Que, L.; Chen, C.; Yue, K. Grey relational analysis–based composite coating property optimization fabricated by laser cladding. *Int. J. Adv. Manuf. Technol.* **2022**, *120*, 7985–7996. [CrossRef]
5. Shi, C.; Lei, J.; Zhou, S.; Dai, X.; Zhang, L.-C. Microstructure and mechanical properties of carbon fibers strengthened Ni-based coatings by laser cladding: The effect of carbon fiber contents. *J. Alloys Compd.* **2018**, *744*, 146–155. [CrossRef]
6. Sun, S.T.; Fu, H.G.; Ping, X.L.; Guo, X.Y.; Lin, J.; Lei, Y.P.; Wu, W.B.; Zhou, J.X. Formation mechanism and mechanical properties of titanium-doped NbC reinforced Ni-based composite coatings. *Appl. Surf. Sci.* **2019**, *476*, 914–927. [CrossRef]
7. Tan, C.; Zou, J.; Wang, D.; Ma, W.; Zhou, K. Duplex strengthening via SiC addition and in-situ precipitation in additively manufactured composite materials. *Compos. Part B Eng.* **2022**, *236*, 109820. [CrossRef]
8. Li, W.; Yang, X.; Xiao, J.; Hou, Q. Effect of WC mass fraction on the microstructure and friction properties of WC/Ni60 laser cladding layer of brake discs. *Ceram. Int.* **2021**, *47*, 28754–28763. [CrossRef]
9. Zhao, Y.; Feng, K.; Yao, C.W.; Li, Z.G. Effect of MoO_3 on the microstructure and tribological properties of laser-clad Ni_{60}/nanoCu/h-BN/MoO_3 composite coatings over wide temperature range. *Surf. Coat. Technol.* **2020**, *387*, 125477. [CrossRef]
10. Zhu, Z.; Li, J.; Peng, Y.; Shen, G. In-situ synthesized novel eyeball-like Al_2O_3/TiC composite ceramics reinforced Fe-based alloy coating produced by laser cladding. *Surf. Coat. Technol.* **2020**, *391*, 125671. [CrossRef]

11. Yang, C.; Cheng, X.; Tang, H.; Tian, X.; Liu, D. Influence of microstructures and wear behaviors of the microalloyed coatings on TC11 alloy surface using laser cladding technique. *Surf. Coat. Technol.* **2018**, *337*, 97–103. [CrossRef]
12. Li, X.; Liu, S.; Wang, J.; Yu, M.; Tang, H. Effect of Different ZrN Addition on Microstructure and Wear Properties of Titanium Based Coatings by Laser Cladding Technique. *Coatings* **2019**, *9*, 261. [CrossRef]
13. Yong, Y.-W.; Fu, W.; Deng, Q.-L.; Yang, J.-G. Mechanism of Zr in in situ-synthesized particle reinforced composite coatings by laser cladding. *Rare Met.* **2017**, *36*, 934–941. [CrossRef]
14. Guo, C.; Zhou, J.; Zhao, J.; Chen, J. Effect of ZrB_2 on the Microstructure and Wear Resistance of Ni-Based Composite Coating Produced on Pure Ti by Laser Cladding. *Tribol. Trans.* **2010**, *54*, 80–86. [CrossRef]
15. Liu, K.; Li, Y.; Wang, J.; Ma, Q. In-situ synthesized Ni–Zr intermetallic/ceramic reinforced composite coatings on zirconium substrate by high power diode laser. *J. Alloys Compd.* **2015**, *624*, 234–240. [CrossRef]
16. Zhu, S.; Chen, W.; Zhan, X.; Ding, L.; Wang, E. Optimization of dilution rate of laser cladding repair based on deep learning. *Int. J. Adv. Manuf. Technol.* **2020**, *110*, 1471–1484. [CrossRef]
17. Rui, H.; Meiping, W.; Chen, C.; Dadong, J.; Yuling, G.; Xiaojin, M. Microstructure evolution, mechanical properties of FeCrNiMnAl high entropy alloy coatings fabricated by laser cladding. *Surf. Coat. Technol.* **2022**, *447*, 128851. [CrossRef]
18. Cui, C.; Wu, M.; Miao, X.; Gong, Y.; Zhao, Z. The effect of laser energy density on the geometric characteristics, microstructure and corrosion resistance of Co-based coatings by laser cladding. *J. Mater. Res. Technol.* **2021**, *15*, 2405–2418. [CrossRef]
19. Ghasempour-Mouziraji, M.; Limouei, M.B.; Najafizadeh, M.; Hosseinzadeh, M.; Cavaliere, P. The effect of simple shear extrusion on the mechanical properties and microstructure of copper. *Mater. Lett.* **2023**, *335*, 133815. [CrossRef]
20. Liu, K.; Li, Y.; Wang, J.; Ma, Q. Effect of high dilution on the in situ synthesis of Ni–Zr/Zr–Si(B, C) reinforced composite coating on zirconium alloy substrate by laser cladding. *Mater. Des.* **2015**, *87*, 66–74. [CrossRef]
21. Berretta, S.; Wang, Y.; Davies, R.; Ghita, O.R. Polymer viscosity, particle coalescence and mechanical performance in high-temperature laser sintering. *J. Mater. Sci.* **2016**, *51*, 4778–4794. [CrossRef]
22. Song, G.-M.; Wang, Y.-J.; Zhou, Y. The mechanical and thermophysical properties of ZrC/W composites at elevated temperature. *Mater. Sci. Eng. A* **2002**, *334*, 223–232. [CrossRef]
23. Yu, T.; Deng, Q.; Dong, G.; Yang, J. Effects of Ta on microstructure and microhardness of Ni based laser clad coating. *Appl. Surf. Sci.* **2011**, *257*, 5098–5103. [CrossRef]
24. Zhang, T.; Wang, Y.; Zhou, Y.; Song, G. Effect of temperature gradient in the disk during sintering on microstructure and mechanical properties of ZrC.sub.p/W composite. *Int. J. Refract. Met. Hard Mater.* **2009**, *27*, 126. [CrossRef]
25. Kim, J.-H.; Park, C.; Ha, D.; Kang, S. WC-toughened (Zr,W)C solid solution carbides. *J. Alloys Compd.* **2015**, *637*, 183–187. [CrossRef]
26. Yang, L.; Yu, T.; Li, M.; Zhao, Y.; Sun, J. Microstructure and wear resistance of in-situ synthesized Ti(C, N) ceramic reinforced Fe-based coating by laser cladding. *Ceram. Int.* **2018**, *44*, 22538–22548. [CrossRef]
27. Kharanzhevskiy, E.V.; Ipatov, A.G.; Makarov, A.V.; Gil'mutdinov, F.Z.; Soboleva, N.N.; Krivilyov, M.D. Effect of oxygen in surface layers formed during sliding wear of Ni–ZrO_2 coatings. *Surf. Coat. Technol.* **2022**, *434*, 128174. [CrossRef]
28. Deng, X.; Huang, L.; Wang, Q.; Fu, T.; Wang, Z. Three-body abrasion wear resistance of TiC-reinforced low-alloy abrasion-resistant martensitic steel under dry and wet sand conditions. *Wear* **2020**, *452–453*, 203310. [CrossRef]
29. Yazdani, S.; Vitry, V. Using Molecular Dynamic Simulation to Understand the Deformation Mechanism in Cu, Ni, and Equimolar Cu-Ni Polycrystalline Alloys. *Alloys* **2023**, *2*, 77–88. [CrossRef]